Physica Scripta

PAPER

Machine learning-assisted prediction of the electronic features of a Schottky diode interlaid with PVP:$BaTiO_3$ composite

Yashar Azizian-Kalandaragh[1,2,3], **Ali Barkhordari**[4,*], **Süleyman Özçelik**[1,2] **and Şemsettin Altındal**[5]

[1] Department of Photonics, Faculty of Applied Sciences, Gazi University, 06500, Ankara, Turkey
[2] Photonics Application and Research Center, Gazi University, 06500, Ankara, Turkey
[3] Department of Physics, University of Mohaghegh Ardabili, PO Box.179, Ardabil, Iran
[4] Faculty of Physics, Shahid Bahonar University of Kerman, Kerman, Iran
[5] Department of Physics, Faculty of Sciences, Gazi University, Ankara, Turkey
[*] Author to whom any correspondence should be addressed.

E-mail: yashar.a.k@gmail.com **and** alibarkhordari20@yahoo.com

RECEIVED
10 April 2024

REVISED
21 June 2024

ACCEPTED FOR PUBLICATION
28 June 2024

PUBLISHED
9 July 2024

Keywords: Schottky type diode, barium titanate ($BaTiO_3$) nanoparticles, electronic specifications, nanocomposite interlayer, machine learning algorithms

Abstract

This study employs two Machine Learning (ML) models to predict the electronic current and then analyze the main electronic variables of Schottky diodes (SDs), including leak current (I_0), potential barrier height (Φ_{B0}), ideality factor (n), series resistance (R_s), shunt resistance (R_{sh}), rectifying ratio (RR), and interface states density (N_{ss}). The I-V characteristics are examined for both without and with an interlayer. The polyvinylpyrrolidone (PVP) polymer and $BaTiO_3$ nanostructures are combined to form the nanocomposite interface. The ML algorithms that are employed include the Gaussian Process Regression (GPR) and Kernel Ridge Regression (KRR). The thermionic emission theory is used to gather training data for ML algorithms. Ultimately, the effectiveness of these ML methods in anticipating the electric characteristics of SDs is evaluated by contrasting the predicted and experimental findings in order to identify the optimal ML model. Whereas the GPR algorithm has given values that are closer to the actual values, the ML predictions of fundamental electric variables by practically both algorithms have the best level of agreement with the actual values. Also, the obtained findings indicate that when the nanocomposite interface is used, the amount of I_0 and N_{ss} for metal-semiconductor (MS) Schottky diodes reduces and φ_{B0} increases.

1. Introduction

A Schottky diode (SD) with a structure of metal-semiconductor (MS) in absence or presence of an interfacial layer has been classified as a rectification or non-rectification instrument based on the potential barrier height (BH) value [1]. Once the height amount of the electric potential barrier is sufficiently vast or small, the joint is either ohmic or Schottky [2–5].

The ohmic and rectifying behavior of these devices are also determined by the foreside metallic rectifying contacts, the value of the work function corresponding to the semiconductor employed, and the back metal ohmic, according to Schottky and Mott theory [1, 4, 5]. The value of the metal work function (Φ_m) in a p-type semiconductor has to be smaller than the value of the semiconductor work function (Φ_s) to produce a rectifier; nevertheless, $\Phi_m > \Phi_s$ to produce an ohmic contact. The scenario is inverted for an n-type semiconductor.

These configurations are crucial to all semiconductor devices, including solar cells, capacitors, transistors, and SD with or without a polymer interlayer [3]. The main scientific and manufacturing challenge with MS configurations is that their increasing efficacy and economically viable production depend on the appropriate use of large-dielectric materials and metal/metal-oxide dopants in combination with a variety of interfacial polymer/organic layers [3–7].

Put another way, achieving both cost and performance reductions is now the biggest technological challenge. Since polymers typically have low conductivity and dielectric properties but great mechanical and dynamic strength, they are inexpensive, flexible, and easy to build. But by using a small amount of metallic and metallic-oxide elements as dopants into them, this issue may be solved. Consequently, it is important to note that the traditional insulator layers that were created using antiquated methods and put between metal and semiconductor layers were unable to passivate the dangling bonds, activating on the semiconductor surface and lower the leak current [6–11].

Improved optical, electronic, and dielectric characterizations of the MS instruments interlaid with a polymer/organic layer without/with dopants of metallic, metallic oxide, and graphene nanoparticles can also be attributed to factors like appropriate stableness of mechanical and dielectric specifications, great storage capacity of charge/energy, simplicity process methods, small weight, and sufficient flexibility [12–15]. Therefore, in order to improve the efficacy of the MS configuration, potential BH needs to be controlled and manipulated.

The application of SDs in electronics technology is influenced by their electrical response, which varies based on the operating environment. In addition, the determination of electronic properties of SDs is a long-time and expensive procedure because of needing the sensitive lab. Therefore, a high reliability engineering techniques are necessary that have a capability to anticipate the electronic characteristics of SDs. However, there are occasionally notable differences between the theoretical and experimentally observed electrical characteristics utilizing thermionic emission theory that deviate significantly from the ideal condition.

The R_s quantity of a diode, the surface/interface states/traps (D_{it}/N_{ss}) produced amidst the semiconductor and interfacial layer, the non-uniformity of the electric potential barrier and the interlayer deposited at the M/S interface, and other factors are often responsible for these discrepancies. As a result, it makes sense to use other techniques that can cut down on the number of experiments conducted, saving money and effort [12, 16, 17]. Machine learning (ML) is currently the most popular approach to achieving this goal. Research has demonstrated the usefulness of ML methods in the field of Schottky configurations and the prediction of several electronic features of them, in addition to proving that ML is applicable in most scientific and technological domains. One area of artificial intelligence called machine learning (ML) is capable of analyzing data samples and developing regulations and patterns to expand a simulation algorithm for the purpose of anticipating new data. It is a potent, highly accurate prediction tool that is used in many sectors and eliminates the need for human judgement and middlemanship. To learn the rules and subsequently forecast fresh data, machine learning (ML) uses a wide variety of modelling methods [13]. In recent times, the Machine Learning (ML) approach has been employed in the literature to analyze the electrical properties of SDs.

Using four machine learning techniques, Torun *et al* [14] examined the I-V measurements of Au/Ni/n-GaN SD at the temperature range of 40–400 K. The sample with the experiment data of 5192 was modelled using the Support Vector Regression (SVR), Gaussian Process Regression (GPR), Artificial Neural Network (ANN), and Adaptive Neuro Fuzzy System (ANFS) methods. When they compared the models' performance with one another after collecting the model error, they discovered that, out of all the models used, the AFNS approach had the best efficacy at the train and test steps. Based on the experimental results, Ali *et al* [15] used an artificial neural network (ANN) to estimate the electronic current of the prepared SDs depending on temperature and voltage applied. They demonstrated how the I-V values that the ANN model predicted accord well and with an acceptable accuracy with the experimental data. The electronic current prediction of 6H-SiC/MEH-PPV SDs depending on the applied voltage and temperature was reported by Güzel *et al* [18] using an ANN algorithm. The temperature and voltage ranges used to measure the experimental results were 100–250 K and −3 V to +3 V, respectively. With an average variance of 0.15% and high accuracy, the outcomes predicted by the ANN system do not match the experimental ones.

For capacitors, MIS-type SDs, and solar cell applications, an interfacial layer developed between metal and semiconductor might be thought of as $BaTiO_3$ nanocomposite [19–21]. To improve the electrical performance of the MS-type SD, barium-titanate nanoparticles have been used for doping the PVP layer as an interface amidst the Aluminum and p-type silicon layers in this work. To investigate the impact of this interfacial nanocomposite layer on the fundamental electric properties of the MS Schottky diode, two SDs with the architectures of Al/p-Si (MS) and Al/PVP:$BaTiO_3$/p-Si (MPS) have been produced. The methods for preparing the materials and fabricating the SDs have been succinctly described. Subsequently, the TE approach was used to analyze the SDs' I-V measurements of the fabricated SDs, which allowed for the computation and analysis of the primary electric parameters, including I_0, n, BH, R_s, R_{sh}, and RR. Next, the I-V characteristics will be predicted using the Gaussian Process Regression (GPR) and Kernel Ridge Regression (KRR) algorithms of the ML technique, and further electrical parameters of the SDs as well as and the energy dependence of the interface states density will be computed. The effectiveness of the various ML models for precisely anticipating the electronic characteristics of SDs has been assessed by comparing the experimental and predicted findings in order to determine the performance of the ML method.

2. Experimental details

2.1. Materials & devices

Using titanium tetrachloride ($TiCl_4$), barium carbonate ($BaCO_3$), and sodium hydroxide (NaOH) manufactured by Merk (German company) as precursors, the barium titanate ($BaTiO_3$) nanoparticles and Al/PVP: $BaTiO_3$/p-Si SD were created. The microwave device, manufactured by Samsung (a Korean company), had a power range from 100 W to 800 W and a frequency of 2450 MHz. The Al/PVP: $BaTiO_3$/p-Si SD was created using a spin coater technique, p-type silicon wafer, polyvinyl pyrrolidine (PVP). In addition, the silicon wafers have been washed using ethanol (C_2H_5OH), methanol (CH_3OH), acetone (CH_3COCH_3), hydrogen peroxide (H_2O_2), and hydrofluoric acid (HF).

A scanning electron microscope (SEM) (model LEO 1430 VP) that operates at an accelerator voltage of 15 kV and a Philips X pert device with Cu k_α radiation (1.55 angstrom wavelength) were used to examine the surface morphology and structural characterization of the $BaTiO_3$ nanostructures. Moreover, KEITHLEY (Model 2450) measured the I-V characteristic of the manufactured SDs at room temperature.

2.2. Preparation of $BaTiO_3$ nano-powder & SD

By taking into account the stoichiometric proportions of the processes, a 20^{cc} solution containing 0.2 molar of barium carbonate ($BaCO_3$), sodium hydroxide (NaOH), and titanium dioxide (TiO_2) precursors was created at 3 beakers individually to synthesize barium titanium. Using ultrasonic irradiation, dropwise additions of sodium hydroxide (NaOH) and titanium dioxide (TiO_2) solutions were made to the bismuth nitrate ($Ba(NO_3)_3$) solution at this stage. Note that in this step, the pH of the solution was 13. The solution was then exposed to a 10-minute microwave radiation exposure at 800 W of power. The yellow mixture that was produced was then dried at room temperature and washed for five minutes with deionized water. A barium titanate nanostructure was created by placing the solid powder that had been produced in a furnace set at 700 °C for two hours in order to eliminate the water molecules.

2.3. Rinsing p-Si wafer

It needs to clear the silicon wafer surface from impurities and the intrinsic silicon dioxide layer must be removed for preparing the surface for covering the nanocomposite layer and creating a MPS SD. The silicon wafer should thus be washed with various liquids. In this research, the Si wafer has been rinsed three times: once at 55 °C for five minutes using a mixture of acetone and methanol; once at 70 °C for fifteen minutes using a mixture of NH_4OH, water H_2O, and H_2O_2. Lastly, once at room temperature for two minutes, using a combination of water H_2O and HF.

2.4. Fabricating MS- and MPS-type SDs

The Al/PVP: $BaTiO_3$ structure is deposited onto a p-type Si wafer, a one crystal at the plane of (100) with a resistance of 1–10 $\Omega.cm^{-1}$, thickness of 300 μm. To produce an appropriate ohmic contact, a 100 nm thick coating of aluminum was sprayed using the sputtering method at 1 μTorr pressure on the underside of the silicon wafer. The layer was then annealed at 500 °C. Additionally, a spin coater technique was used to produce a thin layer of 100 nm-thick PVP:$BaTiO_3$ nanocomposite on the silicon wafer's upside surface. Ultimately, masks with a 1.2 mm diameter and 100 nm thickness were used to deposit the ohmic joints in circular form onto the PVP:$BaTiO_3$ nanocomposite layer. Consequently, two SDs were created using the MPS contact of Al/PVP: $BaTiO_3$/p-Si and the MS contact of Al/p-Si. Figure 1 displays a schematic of the manufactured SD with PVP:$BaTiO_3$ nanocomposite interlayer.

2.5. XRD analysis

Figure 2 displays the $BaTiO_3$ nanostructures' XRD pattern, which has been produced with the use of a microwave. Analyzing the x-ray diffraction pattern reveals that the perovskite-type $BaTiO_3$ structure has formed. The crystalline plane introduced in figure 2 are respectively related to the angles of 22.3°, 31.7°, 39.7°, 44.4°, 45.5°, 49.2°, 56.5° and 65.5°. The appearance of the crystalline planes (002) and (200) demonstrates a tetragonal symmetry in the $BaTiO_3$ crystal [19, 20]. It is necessary to mention that other peaks that appeared in the XRD pattern correspond to the $BaCO_3$ and TiO_2 crystals that exist in the compound as impurities [21–23]. Using the Debye–Scherrer equation, the mean size of $BaTiO_3$ crystal can be determined as [23]:

$$D = k\lambda/\beta \cos\theta \quad (1)$$

where λ is the x-ray wavelength, which is equal to 15.4056 nm, β is the FWHM of the selected peak in the XRD, θ refers to the Bragg angle, and D being the crystallite size [23]. Equation (1) yields an average size of 30 nm for the $BaTiO_3$ crystal. It is important to remember that lattice faults like as dislocations, displacements, and impurities create stress in the crystal lattice, which results in peak broadening and intensification. The Williamson–Hall

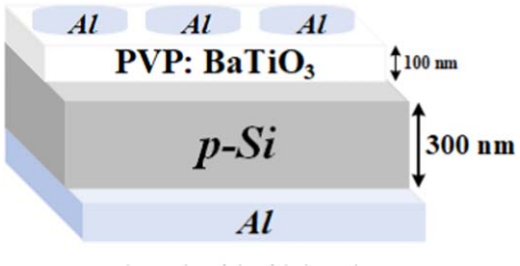

Figure 1. Schematic of the fabricated MPS-type SD.

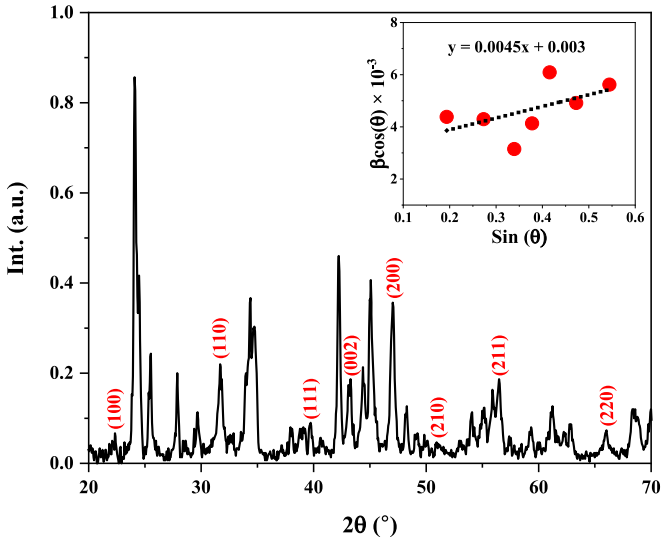

Figure 2. XRD spectrum of the $BaTiO_3$ nanoparticles.

relation, which can be represented as follows, was used to compute the strain value arising from lattice stress and the mean size of the crystallites [22],

$$\beta \cos(\theta) = \varepsilon \sin(\theta) + \frac{k\lambda}{D} \tag{2}$$

The strain parameter is represented by ε in this case, and the remaining variables are the same as in equation (1). It is able to determine the strain value and average crystalline size of the $BaTiO_3$ nanoparticles, which was approximately 1.13×10^{-3} and 48 nm, respectively, by using the previously established relation and the slope and intercept quantities of the $\beta\cos(\theta)$-$\sin(\theta)$ linear graph (see the inset of figure 2).

2.6. SEM analysis

Using the microwave approach, FE-SEM pictures have been captured in order to analyze the morphology of the generated $BaTiO_3$ nanoparticles. The surface morphological schemes of the synthesized $BaTiO_3$ nanoparticles, as determined by SEM test, are displayed in figure 3. While genuine particle sizes are difficult to visualize, the creation of agglomerated and polydispersity nanoparticles with a range of shapes are able to see. Each nanoparticle is observed to have a distinct shape, with a mean size of roughly 70 nm and a mean cluster size of smaller than 1 μm.

3. ML algorithms

As a significant area of artificial intelligence, machine learning is an interdisciplinary field grounded in computer science, mathematics, statistics, and engineering. Its goal is to optimize computer programmers' performance through the use of data and past experiences. Many similar studies show that using machine learning to quickly extract rules and trends from obtainable data is a useful approach, as it eliminates the need for expensive experiments and physical mechanisms. Many scientific and engineering challenges, including those in computer

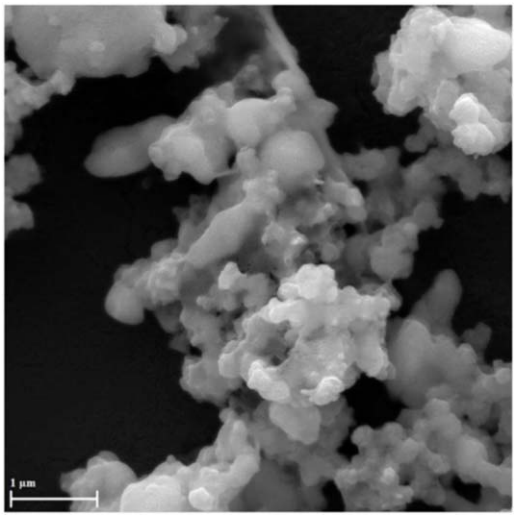

Figure 3. SEM picture of the synthesized $BaTiO_3$ nanoparticles.

vision, physics, chemistry, biology, medicine, industry, and even finance, have made use of machine learning, according to recent studies [24–34]. In this research, the I-V diagram is modelled and some electrical properties of Schottky structures are predicted using some of ML approaches, including GPR and KRR. Next, the outcomes of the aforementioned algorithms are contrasted with the experimental data and with one another. We provide a brief explanation of the algorithms utilized in this paper below.

3.1. GPR model

The GPR model is a supervised ML method that is non-parametric and employs a probabilistic interpretation of data [35]. GPR models offer a potent tool for result prediction because it is believed that the outputs have a combined Gaussian distribution [36]. As a result, the possibility distribution of the anticipated factors provided in the learning data can be estimated to frame the GPR problem. It can specify the outputs' joint probability distribution as follows:

$$\begin{pmatrix} Y \\ Y_p \end{pmatrix} \sim \mathcal{N}(0,\ \delta) \tag{3}$$

Where $\mathcal{N}$ denotes the Gaussian distribution function that has an average amount of **0** and a covariance matrix of δ. Without sacrificing generality, the joint distribution's average value will be assumed to be zero. That being said, even in cases where the output distribution revolves around a non-zero mean, the zero average value can be subtracted from the joint distribution to satisfy the assumption. The covariance matrix, δ, is provided by;

$$\delta = \begin{pmatrix} \mathrm{K} & \mathrm{K}_* \\ \mathrm{K}_*^{\mathrm{T}} & \mathrm{K}_{**} \end{pmatrix} \tag{4}$$

The individual covariance matrices, which are composites of the training and test data sets, are denoted by the elements K, K_*, and K_{**}. The kernel function that is positive definite describes the covariance matrix elements, K, as:

$$\mathrm{K}(\mathbf{x},\ \mathbf{x}') = -\lambda \exp\left(\frac{1}{2\sigma^2} \|\mathbf{x} - \mathbf{x}'\|_2^2\right) \tag{5}$$

where x and x' are the input pairs subordinate to the appropriate data sets, and σ and λ stand for the GPR model's hyperparameters. In actuality, the kernel function measures how similar or how far apart the input pairs are from one another. Based on the training data, the GPR seeks to anticipate the new distribution of the test data. It is important to note that GPR is a non-parametric function, in contrast to linear regression. GPR's non-parametric characteristics enable it to forecast non-linear behaviors. Furthermore, the GPR algorithm gives confidence boundaries on the model's predictions by providing an associated variance in addition to the expected value of the forecast. GP actively uses the training data to create predictions, instead than depending just on it [35].

3.2. KKR algorithm

One of the simple techniques that can be kernelized is ridge regression. To do this, a linear function representing the dependence of the response variable, $\{y_i\}$, and the continuous covariates, $\{x_i\}$, must be found. The traditional approach to do that is to minimize the quadratic cost as follows [37]:

$$C(\boldsymbol{w}) = \frac{1}{2}\sum_i (y_i - \boldsymbol{w}^T \boldsymbol{x}_i)^2 \tag{6}$$

once working in the feature space, $\phi(x_i)$ should be used instead of the variable x_i. But it increases the chance of encountering overfit, therefore regularizing its avoidance is necessary. A good regularization strategy is the penalizing the size of the weights (**w**). Some of the methods that are used most frequently include leave-one-out estimations and cross-validation. Thus, the following is the total loss function that needs to be minimized [37]:

$$C = \frac{1}{2}\sum_i (y_i - \boldsymbol{w}^T \boldsymbol{x}_i)^2 + \frac{1}{2}\lambda \|\boldsymbol{w}\|^2 \tag{7}$$

By taking the gradients and putting them equal to zero, the following expression may be obtained:

$$\sum_i (y_i - \boldsymbol{w}^T \boldsymbol{x}_i)\boldsymbol{x}_i = \lambda \boldsymbol{w} \Rightarrow \boldsymbol{w} = \left(\lambda \mathbf{I} + \sum_i \boldsymbol{x}_i \boldsymbol{x}_i^T\right)^{-1}\left(\sum_j y_j \boldsymbol{x}_j\right) \tag{8}$$

It is evident that by preventing the lowest eigenvalues from becoming zero, the regularization term leads to the numerical stabilization of the inverse. Once every data point is substituted with its corresponding feature vector, so that $x_i \rightarrow \phi_i = \phi(\boldsymbol{x}_i)$, the number of dimensions will significantly exceed the number of data points. It can do this by utilising a sophisticated strategy that minimizes the amount of data points or the dimensionality of the feature space in order to do the inverse as efficiently as feasible. The method is provided using the following identity as [38]:

$$(P^{-1} + B^T R^{-1} B)^{-1} B^T R^{-1} = PB^T (BPB^T + R)^{-1} \tag{9}$$

with consideration of $\boldsymbol{y} = y_i$ and $\phi = \phi_{ai}$, the solution is given by:

$$w = (\lambda \mathbf{I_d} + \phi\phi^T)^{-1}\phi \boldsymbol{y} = \phi(\phi^T\phi + \lambda \mathbf{I_n})^{-1}\boldsymbol{y} \tag{10}$$

An alternative way to state this equation is as $\boldsymbol{w} = \sum_i \alpha_i \phi(\boldsymbol{x}_i)$ with $\alpha = (\phi^T\phi + \lambda \mathbf{I_n})^{-1}\boldsymbol{y}$. It needs to be proven that it doesn't genuinely need accessibility to the feature vectors-which can be infinitely lengthy. In practice, we need the anticipated value for a recent test case, **x**, which is ascertained by projecting it onto the solution, **w**.

$$y = \boldsymbol{w}^T \phi(\boldsymbol{x}) = \boldsymbol{y}(\phi^T\phi + \lambda \mathbf{I_n})^{-1}\phi^T\phi(x) = y(K + \lambda \mathbf{I_n})^{-1}\boldsymbol{\kappa}(\boldsymbol{x}) \tag{11}$$

With definition of $K(bx_i, bx_j) = \phi^T(x_i)\phi(x_j)$ and $\boldsymbol{\kappa}(\boldsymbol{x}) = K(\boldsymbol{x}_i, \boldsymbol{x})$ [32]. Thus, just find the kernel K is necessary. There are other kernel functions as well, including sigmoid, polynomial, linear, and Radial Basis Function (RBF), the latter of which has been chosen for this research due to its lower component count and numerical complexity [39].

3.3. Error and accuracy functions

As previously mentioned, when the ML model design is finished, a thorough investigation of prediction competency is required. Additionally, the performance variables' computation and subsequent analysis aid in our comprehension of the forecast accuracy. Therefore, to specify the examination accuracy of the ML models utilized in this paper, the functions of mean absolute error (MAE) and mean squared error (MSE), which are expressed as follows [40]:

$$MAE = \frac{1}{N}\sum_{i=1}^{N} |X_{\exp(i)} - X_{pred(i)}| \tag{12}$$

$$MSE = \frac{1}{N}\sum_{i=1}^{N} (X_{\exp(i)} - X_{pred(i)})^2 \tag{13}$$

The R2 score is one of the additional metrics that illustrates the algorithm's correctness. In general, the closer the R2 score is to one, the better the model's training and selection of hyperparameters inside the algorithm, resulting in predictions with lower mean square error (MSE). The model would perform poorly on an unknown dataset if the R2 score was zero, which would be the result of poor hyperparameter selection. When the R2 score value is one, the model is considered flawless. It is computed as follows [41]:

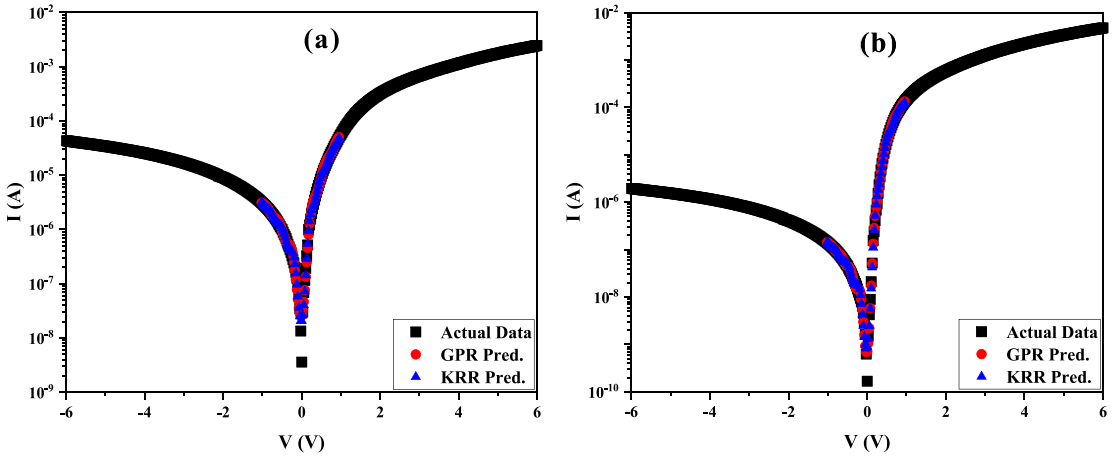

Figure 4. I–V characteristic curves of (a) MS and (b) MPS SDs and their analysis with the GPR and KRR models.

Table 1. The values error and accuracy functions of considered algorithms in prediction of the electric current of the fabricated SDs.

ML Mods. / SD	GPR				KRR			
	MAE	MSE	RMSE	R2_Score	MAE	MSE	RMSE	R2_Score
MS	0.0607	0.0153	0.1236	0.9800	0.0515	0.0118	0.1086	0.9846
MPS1	0.0493	0.0101	0.1005	0.9958	0.0640	0.0137	0.1171	0.9943

$$R2\ \text{Score} = 1 - \frac{\sum_{i=1}^{N}(X_{pred\,(i)} - X_{\exp\,(i)})^2}{\sum_{i=1}^{N}(\bar{X}_{\exp\,(i)} - X_{\exp\,(i)})^2} \tag{14}$$

where X_{exp} represents the experimental value (actual value), X_{pred} is the model's predicted value, and $\bar{X}_{exp}$ is the mean amount of the experimental data. The MAE value of the considered algorithms used to predict the current value of SDs with and without interlayer are represented in table 1. Each algorithm's MAE values have been assessed in relation to 1. It is clear that in the present prediction of SDs, the KRR model's MAE value for the MS-type SD is lower than that of the GPR model while for MPS-type SD, the situation is opposite. Similar behavior is observed in the MSE and RMSE quantities. It is obvious that the differences between them between the error functions value at the SDs are negligible, with these values being quite near to one another. Besides, the R2 score value for both algorithms are close to unit, showing they have managed the prediction well (see table 1). The value of R2 score for the prediction of electric current into the MPS-type SD is slightly higher than that of the MS one.

4. Results and discussion

Figure 4 displays the semilogarithmic diagram of I-V measurements for the constructed SDs without/with $BaTiO_3$ nanocomposite interlayer by using experimental data at ±6 V, GPR, and KRR at ±1 V. In this work, the data was divided into+ three sets: train set (70%), test set (20%), and validation set (10%). Since the number of all data was 481, the test size at utilized algorithms was 97, chosen to ensure predictions at a voltage range from −1 V to +1 V. In addition, the thermionic emission (TE) theory is used to ascertain the I-V data of the manufactured SDs since, in contrast to other techniques like Norde and Cheung, the ML method requires a comparatively large quantity of data in order to properly predict the new data. It's important to note that the foundation of TE hypothesis is the notion that the BH must be significantly larger than kT, which means that only electrons with sufficient energy to cross the electric potential barrier are included in the computation of the current density. Furthermore, it is assumed that thermal equilibrium has been reached at the plane that controls emission, and that the equilibrium is unaffected by the existence of a net current flow [42]. It can be observed that the GPR model, in contrast to KRR algorithm, is more accurate in anticipating the electronic current of

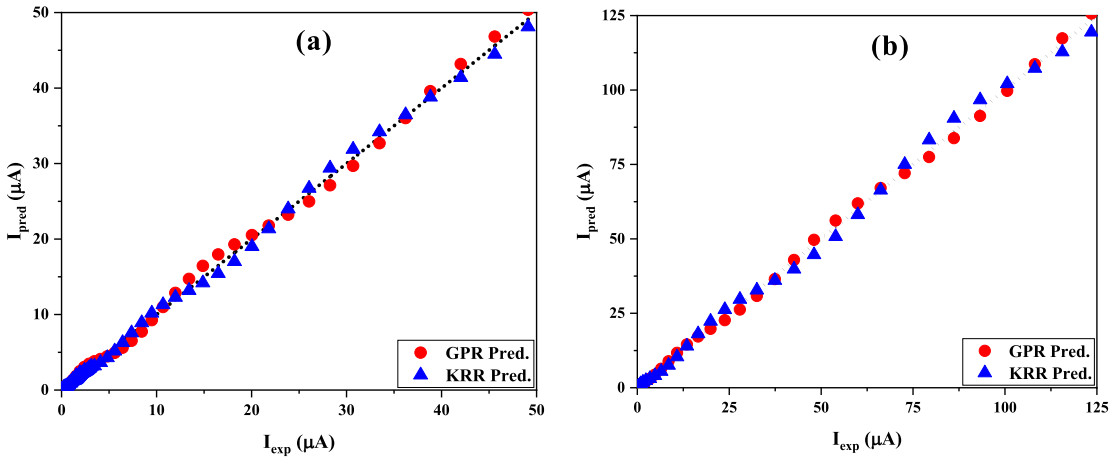

Figure 5. The prediction quantities of the GPR and KRR models for (a) MS- and (b) MPS-type SDs.

Table 2. The actual and prediction quantities of I_0 for the fabricated SDs.

SD \ I_0 (A)	Actual	GPR	KRR
MS	2.0505×10^{-7}	2.2414×10^{-7}	2.5731×10^{-7}
MPS1	1.4200×10^{-8}	1.7035×10^{-8}	1.8398×10^{-8}

MPS-type SD at different biases and validating their MSE values. The situation is opposite for the MS-type SD (see table 1).

Figure 5 simultaneously displays the actual and predicted quantities for each SD without and with nanocomposite interlayer so that the prediction efficacy of the GPR and KRR models may be compared with one another. The x- and y-axes, respectively, show the location of the experimental and output data. In order to provide a more thorough knowledge of prediction accuracy, data point positions must be estimated. To better examine the situation of the data points, the zero-error line was drawn in figure 5 for this purpose. Another indication of the model's ability to predict the electrical current with accuracy is the placement of the data points for the GPR and KRR algorithms with respect to the zero-error line.

The I-V relation in an SD might be written as follows in the forward bias region and by taking a R_s for $V \geqslant 3kT/q$ [21];

$$I = I_0\left[\exp\left(\frac{q(V - IR_s)}{nkT}\right) - 1\right], \tag{15}$$

where T is the temperature, k stands for the Boltzmann constant, and q denotes the electric charge. The linear partition of the ln(I)-V diagram at $V = 0$ yields the value of I_0 as [43]:

$$I_0 = AA^*T^2 \exp\left(-\frac{q\varphi_{B0}}{kT}\right), \tag{16}$$

where its parameters are well-defined in literature [21, 43]. Table 2 introduces both the actual and prediction amounts of I_0 for the fabricated SDs as determined by ML algorithms. It is evident that, among the considered models, the GPR model's predicted value of I_0 is the one that is most similar to the real value. It is worth noting that the amount of I_0 for MS-type SD reduces as the PVP:$BaTiO_3$ interfacial layer is used. It suggests that the PVP polymer-doped $BaTiO_3$ nanoparticles have a great impact on enhancing the electronic characteristics of MS-type SD.

To manage and control the potential BH of the MS SD, a nanocomposite interfacial layer is primarily used. Thus, one of the crucial electronic characteristics of SDs, which needs to be computed at zero-bias voltage, is [44]:

Table 3. The actual and prediction quantities of ΦB_0 for the manufactured SDs.

SD \ Φ_{B0}(eV)	Actual	GPR	KRR
MS	0.7436	0.7413	0.7378
MPS1	0.8127	0.8080	0.8060

Table 4. The actual and prediction amounts of n for the fabricated SDs.

SD \ n	Actual	GPR	KRR
MS	4.6009	4.7362	5.0541
MPS1	2.3680	2.4540	2.4942

$$\varphi_{B0} = \frac{kT}{q} \ln\left(\frac{AA^{*}T^{2}}{I_0}\right). \tag{17}$$

Table 3 contains the BHs of the fabricated SDs that have been acquired. Furthermore, the electronic current needed to determine the BH of various SDs has been modelled using ML methods. In this case, practically every algorithm's prediction and the actual value accord well, however, the values predicted by the GPR model are more matched to the actual data. Physically, once the PVP:$BaTiO_3$ interlayer is placed at the M/S interface, the BH of the MS contact has increased.

One of the key electrical properties of SDs that this research investigates is the ideality factor, which establishes how an SD behaves in relation to the ideality diode. Since a native/deposited interlayer, like insulator, polymer, and ferroelectric materials, are present amidst the M-S layers, its amount is unity in the ideal scenario, but it typically deviates from the ideal circumstances. Additional effective factors in specifying the ideality factor include the density of surface/interface states generated amidst the interlayer/semiconductor, the depletion layer thickness which is defined by the dopant content of donor/acceptor atomic elements into the semiconductor ($W_d = (2\varepsilon_s\varepsilon_o V_i/qN_a)^{0.5}$), the dielectric quantity and thickness of the interlayer. Generally, the slope of ln(I)-V diagram gives the ideality factor as [23, 45]:

$$n = \frac{q}{kT}\left(\frac{dV}{d(lnI)}\right). \tag{18}$$

It is worth mentioning other processes that impact the ideality factor and CTMs/CCMs into the MPS devices include the creation and recombination of e^{-}-h^{+} pairs, electron tunneling through the electric potential barrier with surface states, and barrier lowering due to image-force impact [1, 46]. The computed value of n for the constructed SDs without/with interlayer at the M/S interface is represented in table 4. Its decrease from 4.60 for MS to 2.37 for MPS suggests that the PVP:$BaTiO_3$ interlayer's presence causes the response of SD to near that of the ideal case. Once more, the n quantity for the taken-into-consideration SDs has been anticipated using the ML models. It is clear that the GPR model has excellent accuracy while determining the ideality factor of SDs. The KRR algorithm can predict the n quantity well, but it deviates from the actual values by a larger margin than the GPR model.

One electric property of diodes that influences the rectification ratio (RR) and hence the performance of SDs is series resistance (R_s). The probe wires, the ohmic and rectifying junctions deposited on the foreside and backside of the semiconductor layer, the resistance of the semiconductor, the non-uniformities of the donor/acceptor atomic elements doped in the pure semiconductor, and the leftover contaminations from the cleaning procedure amongst the contacts are some of the sources from which it originated [22, 23, 47]. The R_s will work better in the accumulation zone even though it may be disregarded at the inversion and depletion regions [1, 2]. The value of R_s and R_{sh} are determined in this study using the ohmic law as $R_i = \frac{dV_i}{dI_i}$.

Table 5 introduces the amount of R_s achieved for the constructed SDs without/with the PVP:$BaTiO_3$ interfacial layer at a voltage of +1 V. Additionally, the R_s quantity of the taken-into-consideration SDs is predicted using the ML algorithms. As can be seen, both algorithms' predictions and the actual values coincide rather well; nevertheless, the GPR algorithm is able to predict the R_s amount that corresponds to the actual values with the fewest deviations.

The phenomena such as impurities at the contact region, probe wire-ground patches, and leakage current across the nanocomposite interlayer are the sources of the shunt resistance (R_{sh}) at the reverse bias voltage [47].

Table 5. The actual and prediction quantities of Rs for the fabricated SDs.

SD \ R_s(kΩ)	Actual	GPR	KRR
MS	19.4240	18.9410	19.8915
MPS1	7.2627	7.1588	7.4863

Table 6. The actual and prediction quantities of R_{sh} for the generated SDs.

SD \ R_{sh}(MΩ)	Actual	GPR	KRR
MS	0.3257	0.3268	0.3240
MPS1	7.1658	7.1680	7.1516

Table 7. The actual and prediction amounts of RR for the manufactured SDs.

SD \ RR	Actual	GPR	KRR
MS	16.7689	17.1521	16.3376
MPS1	986.6634	1005.4756	955.6931

Furthermore, given $V_a = V_i + V_{Rs} + V_d + V_{ss}$, the applied voltage ($V_a$) is shared across the MPS SD with R_s and N_{ss}, causing the lnI-V diagram to deviate from the linearity formation for large enough positive voltages [48]. Table 6 represents the quantity of R_{sh} for the produced SDs without/with the $BaTiO_3$ nanocomposite interlayer, computed at ambient temperature and a reverse bias voltage of −1 V. The amount of R_{sh} has been estimated using ML algorithms with varying precisions in comparison of the actual amounts. The R_{sh} value has been predicted by the GPR and KRR models with the least amount of variance from the actual values. The KRR model demonstrates the largest departure from the actual values, while the GPR predictions of the R_{sh} values for the manufactured SDs are nearest to the actual ones. From a physical perspective, the performance of MS-type SD may be improved with a nanocomposite interlayer by significantly increasing the R_{sh} from 0.33 MΩ for the MS SD to 7.17 kΩ for the MPS SD. This leads to a decrease in the leak of oxide/current pathways at the nanocomposite interlayer.

The amount of RR, which may be assessed as the ratio of the electronic current at the positive bias (+1 V) to the negative bias (−1 V) as $RR = I_F/I_R$, determines the rectifying rate of the MS- and MPS-type SD [49]. The RR value of the produced SDs used in this research at ambient temperature is given in table 7. It can be shown that putting the PVP:$BaTiO_3$ interlayer at the M/S interface greatly improves the RR of the MS structure. The anticipated electronic currents at the positive and negative voltages may be utilized to calculate the RR values of various SDs since the ML techniques have anticipated the electronic current of the studied SDs at the voltage range of ±1 V. The highest degree of agreement between the predicted and actual values is seen in the RR values derived from the GPR model's prediction values. However, there is no large difference between the actual values and the values predicted by KRR algorithm.

It is useful to note that the inhomogeneity in the semiconductor's metal/oxide dopant distribution and interface states are two factors contributing to the SD's departure from optimal behavior. The following technique might be applied to comprehend the significance of this defect; N_{ss}'s dependency on voltage applied at the equilibrium state is expressed as [1, 50–52]:

$$N_{ss}(V) = \frac{1}{q}\left[\frac{\varepsilon_i}{\delta}(n(V) - 1) - \frac{\varepsilon_s}{W_D}\right], \tag{19}$$

where W_D stands for the width of depletion layer and δ being and the thick of the nanocomposite interlayer (~100 nm). Additionally, ε_s and ε_i denote the semiconductor/interfacial layer permittivity, in that order. It should be mentioned that the energy differential between a p-type semiconductor's valance band and N_{ss} level is expressed as follows [53]:

Table 8. The actual and prediction quantities of N_{ss} for the fabricated SDs.

SD \ $N_{ss} \times 10^{13}$ ($eV^1.cm^{-2}$)	Actual	GPR	KRR
MS	9.4834	9.4320	9.4615
MPS1	2.2617	2.4031	2.1632

$$E_{ss} - E_v = q(\varphi_e - V). \tag{20}$$

By taking into account the relation among φ_e, R_s, and n(V) might be obtained as [53]:

$$\varphi_e - \varphi_{B0} = \left(1 - \frac{1}{n(V)}\right)V. \tag{21}$$

The N_{ss} values may be computed for the prepared SDs presented in table 8 by using the equations (19)–(21). It is evident that existing a nanocomposite interfacial layer between the semiconductor and metal reduces the density of interface states. This is because the nanocomposite interlayer leads to a passivation on the surface of the semiconductor layer [23]. It should be noted that the transport/conduction mechanisms (CTs/CMs) into the SDs are caused by the formation of potential BH, a native/deposited interlayer amidst the M-S layers, their homogeneous distribution, and surface/interface states density (N_{ss}) [50–54]. Moreover, the N_{ss} value for the fabricated SDs is predicted using ML algorithms. While the predictions of both algorithms show a good level of agreement with the actual quantities, the KRR algorithm predicts values that are identical to the actual values. As such, nearly both ML model taken-into-consideration in this research can accurately predict the N_{ss} quantity.

In the majority of studies conducted in Schottky structures that have applied ML technique, the ANN algorithm has been employed for training and prediction. The acquired results demonstrate that the predicted data nearly approximate the actual data with an insignificant margin of error [14, 15, 18, 55]. In this research, two other algorithms have been utilized, namely GPR and KRR, for training and prediction of the main electrical characteristics of Schottky diodes. Based on the results obtained from ML algorithms, it can be concluded that in all cases, the prediction errors of the GPR and KRR algorithms were very low, and the predicted data closely matched the actual data obtained from experimentation. It is also necessary to pay attention that the determination of hyperparameters plays a crucial role in the implementation of ML algorithms. By choosing the correct and appropriate hyperparameters in an ML algorithm, we can reach the desired goal faster and therefore save more time in the aim execution and achievement. Compared to ANN algorithms, fewer hyperparameters are used in simpler algorithms such as GPR and KRR algorithms. So, these algorithms are easier to use, and algorithm optimization is easier due to having fewer hyperparameters.

5. Conclusions

In order to study the impact of the interfacial nanocomposite layer on the fundamental electronic parameters of the MS SD, two SDs with the architectures of Al/p-Si (MS) and Al/PVP:$BaTiO_3$/p-Si (MPS) were constructed. Subsequently, the TE theory has been employed to examine the I-V measurements of the SDs in order to compute their major electric parameters, including I_0, φ_{B0}, n, R_s, R_{sh}, RR, and N_{ss}. Using ML techniques like GPR and KRR, all of the aforementioned parameters have been predicted and compared to one another. The obtained findings indicate that when the $BaTiO_3$ nanocomposite interlayer is used, the amount of I_0 and N_{ss} for MS-type SD drop, and φ_{B0} rises. Moreover, when the $BaTiO_3$ nanocomposite interlayer is placed between the semiconductor and metal, the BH of the MS contact increases. Therefore, the PVP polymer-doped $BaTiO_3$ nanoparticles have a great effect on improving the electrical specifications of MS-type SD. Also, the respond of SD grows nearer to the ideal situation because of the interfacial nanocomposite layer, as evidenced by the lowering of the n value from 4.60 for MS SD to 2.36 for MPS SD. Additionally, adding an interfacial nanocomposite layer amidst the metal and semiconductor greatly improves the RR of the MS structure. The presence of the PVP polymer layer doped by the $BaTiO_3$ nanoparticles amidst the semiconductor metal causes the interface states density to drop for the MPS structure. The quantities predicted by the KRR model are the furthest from the actual amounts for both MS- and MPS-type SDs, according to a comparison of the actual and predicted quantities of I_0 for fabricated SDs. In contrary, the GPR model had a suitable prediction value of I_0 compared by the actual values for both SDs.

Whereas the GPR model has anticipated amounts that are closer to the actual values, the BH values predicted by nearly both algorithms show high agreement with the actual values. For the variables of n, R_s, and R_{sh}, the prediction performance of both employed methods is almost appropriate. Particularly in the KRR model, their difference between the predicted and actual values is greater than that of the GPR model. Because the ML models

have predicted the electronic current of the fabricated SDs at a voltage range of ±1 V, the computation of RR amounts for both SDs are possible at the positive and negative biases. The KRR model's predicted RR values and the actual values accord the best. Furthermore, the GPR prediction has the highest variance in the RR quantity calculation, but the GPR and KRR predictions have no high divergence from the actual values. For both methods that are utilized, the difference between the predicted and actual values of N_{ss} is sufficiently small.

In summary, nearly both ML techniques considered in this research can accurately predict the N_{ss} value. The predictive capability of both GPR and KRR models for the SDs electronic current is reliable due to the MSE amounts of ML methods. As such, this research can provide insights for future investigations aimed at finding other, more appropriate algorithms and refining and optimizing them to the greatest extent feasible.

Data availability statement

All data that support the findings of this study are included within the article (and any supplementary files).

Conflict of interest

The authors declare no financial or commercial conflict of interest.

ORCID iDs

Yashar Azizian-Kalandaragh https://orcid.org/0000-0001-6181-3767
Ali Barkhordari https://orcid.org/0000-0002-5523-2859

References

[1] Sze S M, Li Y and Ng KK 2021 *Physics of Semiconductor Devices* (Wiley)
[2] Nicollian E H and Brews J R 2002 *MOS (metal oxide semiconductor) physics and technology* (Wiley)
[3] Card H C and Rhoderick E H 1971 Studies of tunnel MOS diodes I. interface effects in silicon Schottky diodes *J. Phys. D: Appl. Phys.* **4** 1589
[4] Tung R T 2014 The physics and chemistry of the Schottky barrier height *Appl. Phys. Rev.* **1** 011304
[5] Al-Ahmadi N A 2020 Metal oxide semiconductor-based Schottky diodes: a review of recent advances *Mater. Res. Express* **7** 032001
[6] Altındal Ş, Barkhordari A, Azizian-Kalandaragh Y, Çevrimli B S and Mashayekhi H R 2022 Dielectric properties and negative-capacitance/dielectric in Au/n-Si structures with PVC and (PVC: Sm2O3) interlayer *Mater. Sci. Semicond. Process.* **147** 106754
[7] Al-Dharob M H, Lapa H E, Kökce A, Özdemir A F, Aldemir D A and Altındal Ş 2018 The investigation of current-conduction mechanisms (CCMs) in Au/(0.07 Zn-PVA)/n-4H-SiC (MPS) Schottky diodes (SDs) by using (IVT) measurements *Mater. Sci. Semicond. Process.* **85** 98–105
[8] Altındal Yerişkin S, Balbaşı M and Orak İ 2017 The effects of (graphene doped-PVA) interlayer on the determinative electrical parameters of the Au/n-Si (MS) structures at room temperature *J. Mater. Sci., Mater. Electron.* **28** 14040–8
[9] Çiçek O, Altındal Ş and Azizian-Kalandaragh Y 2020 A highly sensitive temperature sensor based on Au/graphene-PVP/n-Si type Schottky diodes and the possible conduction mechanisms in the wide range temperatures *IEEE Sens. J.* **20** 14081–9
[10] Reddy V R and Prasad C V 2018 Surface chemical states, electrical and carrier transport properties of Au/ZrO2/n-GaN MIS junction with a high-k ZrO2 as an insulating layer *Materials Science and Engineering: B* **231** 74–80
[11] Ersöz G, Yücedağ İ, Azizian-Kalandaragh Y, Orak I and Altındal Ş 2016 Investigation of electrical characteristics in Al/CdS-PVA/p-Si (MPS) structures using impedance spectroscopy method *IEEE Trans. Electron Devices* **63** 2948–55
[12] Lebda H I, Atyia H E and Habashy D M 2024 From experimentation to prediction: comprehensive study of dielectric properties through experimental research and theoretical modeling *J. Mater. Sci., Mater. Electron.* **35** 1–7
[13] Houssein E H, Abohashima Z, Elhoseny M and Mohamed W M 2022 Machine learning in the quantum realm: the state-of-the-art, challenges, and future vision *Expert Syst. Appl.* **137** 116512
[14] Torun Y and Doğan H 2021 Modeling of Schottky diode characteristic by machine learning techniques based on experimental data with wide temperature range *Superlattices Microstruct.* **160** 107062
[15] Ali H A, El-Zaidia E F and Mohamed R A 2020 Experimental investigation and modeling of electrical properties for phenol red thin film deposited on silicon using back propagation artificial neural network *Chin. J. Phys.* **67** 602–14
[16] Mohamed R A 2022 Modeling of dielectric behavior of polymers nanocomposites using adaptive neuro-fuzzy inference system (ANFIS) *The European Physical Journal Plus* **137** 384
[17] Mohamed R A, El-Nahass M M, El-Bakry M Y, El-Dahshan E S, Aamer E H and Habashy D M 2024 Investigation of optical properties of molybdenum trioxide (MoO3) thin films using neural networks *The European Physical Journal Plus* **139** 378
[18] Güzel T and Çolak A B 2021 Artificial intelligence approach on predicting current values of polymer interface Schottky diode based on temperature and voltage: an experimental study *Superlattices Microstruct.* **153** 106864
[19] Kim H T, Nahm S, Byun J D and Kim Y 1999 Low-fired (Zn, Mg) TiO3 microwave dielectrics *J. Am. Ceram. Soc.* **82** 3476–80
[20] Gui Y, Li S, Xu J and Li C 2008 Study on TiO2-doped ZnO thick film gas sensors enhanced by UV light at room temperature *Microelectron. J.* **39** 1120–5
[21] Durmus Z, Durmus A and Kavas H 2015 Synthesis and characterization of structural and magnetic properties of graphene/hard ferrite nanocomposites as microwave-absorbing material *J. Mater. Sci.* **50** 1201–13
[22] Ashiri R, Nemati A, Ghamsari M S, Sanjabi S and Aalipour M 2011 A modified method for barium titanate nanoparticles synthesis *Mater. Res. Bull.* **46** 2291–5

[23] Barkhordari A, Özçelik S, Altındal Ş, Pirgholi-Givi G, Mashayekhi H and Azizian-Kalandaragh Y 2021 The effect of PVP: BaTiO3 interlayer on the conduction mechanism and electrical properties at MPS structures *Phys. Scr.* **96** 085805
[24] Crampon K, Giorkallos A, Deldossi M, Baud S and Steffenel L A 2022 Machine-learning methods for ligand–protein molecular docking *Drug Discovery Today* **27** 151–64
[25] Chan C H, Sun M and Huang B 2022 Application of machine learning for advanced material prediction and design *EcoMat.* **4** e12194
[26] Xu P, Chen H, Li M and Lu W 2022 New opportunity: machine learning for polymer materials design and discovery *Advanced Theory and Simulations.* **5** 2100565
[27] Tao Q, Xu P, Li M and Lu W 2021 Machine learning for perovskite materials design and discovery *NPJ Comput. Mater.* **7** 23
[28] Liu X, Xu P, Zhao J, Lu W, Li M and Wang G 2022 Material machine learning for alloys: applications, challenges and perspectives *J. Alloys Compd.* 165984
[29] Sabry F, Eltaras T, Labda W, Alzoubi K and Malluhi Q 2022 Machine learning for healthcare wearable devices: the big picture *Journal of Healthcare Engineering* **2022** 46539231
[30] Mueller B, Kinoshita T, Peebles A, Graber M A and Lee S 2022 Artificial intelligence and machine learning in emergency medicine: a narrative review *Acute medicine & surgery* **9** e740
[31] Ivanciuc O 2007 Applications of support vector machines in chemistry *Rev. Comput. Chem.* **23** 291
[32] Doğan H, Duman S, Torun Y, Akkoyun S, Doğan S and Atici U 2022 Neural network estimations of annealed and non-annealed Schottky diode characteristics at wide temperatures range *Mater. Sci. Semicond. Process.* **149** 106854
[33] Güzel T and Çolak A B 2022 Investigation of the usability of machine learning algorithms in determining the specific electrical parameters of Schottky diodes *Materials Today Communications* **33** 104175
[34] Ahmed S, Alshater M M, El Ammari A and Hammami H 2022 Artificial intelligence and machine learning in finance: a bibliometric review *Research in International Business and Finance* **61** 101646
[35] Rasmussen C E and Williams C K 2006 *Gaussian Processes for Machine Learning* (MIT press)
[36] Murphy K P 1991 *Mach. Learn.* (Springer)
[37] Mohri M, Rostamizadeh A and Talwalkar A 2018 *Foundations of machine learning* (MIT press)
[38] Rupp M, Tkatchenko A, Müller K R and Von Lilienfeld O A 2012 Fast and accurate modeling of molecular atomization energies with machine learning *Phys. Rev. Lett.* **108** 058301
[39] Zhang R and Wang W 2011 Facilitating the applications of support vector machine by using a new kernel *Expert Syst. Appl.* **38** 14225–30
[40] Çolak A B, Yıldız O, Bayrak M and Tezekici B S 2020 Experimental study for predicting the specific heat of water based Cu-Al2O3 hybrid nanofluid using artificial neural network and proposing new correlation *Int. J. Energy Res.* **44** 7198–215
[41] Öcal S, Gökçek M, Çolak A B and Korkanç M 2021 A comprehensive and comparative experimental analysis on thermal conductivity of TiO 2-CaCO 3/Water hybrid nanofluid: Proposing new correlation and artificial neural network optimization *Heat Transfer Res.* **52**
[42] Potje-Kamloth K 2002 Chemical gas sensors based on organic semiconductor polypyrrole *Crit. Rev. Anal. Chem.* **32** 121–40
[43] Barkhordari A, Altındal Ş, Pirgholi-Givi G, Mashayekhi H, Özçelik S and Azizian-Kalandaragh Y 2022 The Influence of PVC and (PVC: SnS) interfacial polymer layers on the electric and dielectric properties of Au/n-Si structure *Silicon.* **15** 855–65
[44] Altındal Ş, Sevgili Ö and Azizian-Kalandaragh Y 2019 A comparison of electrical parameters of Au/n-Si and Au/(CoSO4–PVP)/n-Si structures (SBDs) to determine the effect of (CoSO4–PVP) organic interlayer at room temperature *J. Mater. Sci., Mater. Electron.* **30** 9273–80
[45] Vargas O, Caballero Á and Morales J 2014 Enhanced electrochemical performance of maghemite/graphene nanosheets composite as electrode in half and full Li–ion cells *Electrochim. Acta* **130** 551–8
[46] Altındal Ş, Barkhordari A, Özçelik S, Pirgholi-Givi G, Mashayekhi H R and Azizian-Kalandaragh Y 2021 A comparison of electrical characteristics of Au/n-Si (MS) structures with PVC and (PVC: Sm2O3) polymer interlayer *Phys. Scr.* **96** 125838
[47] Ansaree J and Upadhyay S 2015 Thermal analysis of formation of nano-crystalline BaTiO3 using Ba(NO3)2 and TiO2 *Processing and Application of Ceramics* **9** 181–5
[48] Yu P, Cui B and Shi Q 2008 Preparation and characterization of BaTiO3 powders and ceramics by sol-gel process using oleic acid as surfactant *Materials Science and Engineering:* A **473** 34–41
[49] Altındal Ş, Barkhordari A, Pirgholi-Givi G, Ulusoy M, Mashayekhi H, Özçelik S and Azizian-Kalandaragh Y 2021 Comparison of the electrical and impedance properties of Au/(ZnOMn: PVP)/n-Si (MPS) type Schottky-diodes (SDs) before and after gamma-irradiation *Phys. Scr.* **96** 125881
[50] Rahman N *et al* 2021 First principle study of structural, electronic, optical and mechanical properties of cubic fluoro-perovskites: (CdXF3, X = Y, Bi) *The European Physical Journal Plus* **136** 347
[51] Husain M, Rahman N, Khan R, Zulfiqar S, Khattak S A, Khan S N, Sohail M, Iqbal A, Reshak A H and Khan A 2022 Structural, electronic, elastic, and magnetic properties of NaQF3 (Q = ag, Pb, Rh, and Ru) flouroperovskites: a first-principle outcomes *Int. J. Energy Res.* **46** 2446–53
[52] Husain M, Rahman N, Khan R, Sohail M, Khan A A, Elansary H O, El-Abedin T K, Mahmoud E A, Abdelmohsen S A and Khan A 2022 Exploring the exemplary structural, electronic, optical, and elastic nature of inorganic ternary cubic XBaF3 (X = Al and Tl) employing the accurate TB-mBJ approach *Semicond. Sci. Technol.* **37** 075004
[53] Saddique J *et al* 2022 Modeling structural, elastic, electronic and optical properties of ternary cubic barium based fluoroperovskites MBaF3 (M = Ga and In) compounds based on DFT *Mater. Sci. Semicond. Process.* **139** 106345
[54] Husain M *et al* 2022 Examining computationally the structural, elastic, optical, and electronic properties of CaQCl 3 (Q = Li and K) chloroperovskites using DFT framework *RSC Adv.* **12** 32338–49
[55] Çolak A B, Güzel T, Yıldız O and Özer M 2021 An experimental study on determination of the shottky diode current-voltage characteristic depending on temperature with artificial neural network *Physica* B **608** 412852